

ChemComm

Accepted Manuscript



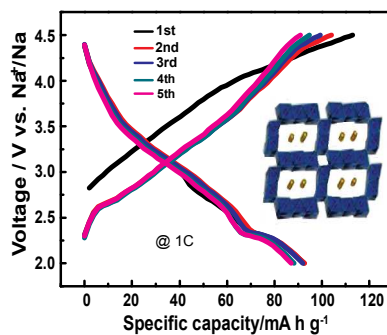
This is an *Accepted Manuscript*, which has been through the Royal Society of Chemistry peer review process and has been accepted for publication.

Accepted Manuscripts are published online shortly after acceptance, before technical editing, formatting and proof reading. Using this free service, authors can make their results available to the community, in citable form, before we publish the edited article. We will replace this *Accepted Manuscript* with the edited and formatted *Advance Article* as soon as it is available.

You can find more information about *Accepted Manuscripts* in the [Information for Authors](#).

Please note that technical editing may introduce minor changes to the text and/or graphics, which may alter content. The journal's standard [Terms & Conditions](#) and the [Ethical guidelines](#) still apply. In no event shall the Royal Society of Chemistry be held responsible for any errors or omissions in this *Accepted Manuscript* or any consequences arising from the use of any information it contains.

The Table of Contents



A new SIB cathode composed of $\text{Na}_{0.31}\text{MnO}_{1.9}$ nanofibers: The nanofibrous $\text{Na}_{0.31}\text{MnO}_{1.9}$ cathode can deliver a sodium-storage capacity of $>100 \text{ mA h g}^{-1}$ at 0.2C with superior high-rate capabilities, good cycling performance and the ability of fast charge.



Journal Name

COMMUNICATION

Romanechite-structural $\text{Na}_{0.31}\text{MnO}_{1.9}$ nanofibers as high-performance cathode material for sodium ion battery

Received 00th January 20xx,
Accepted 00th January 20xx

Jin-Yue Li, Xing-Long Wu,* Xiao-Hua Zhang, Hong-Yan Lü, Guang Wang, Jin-Zhi Guo, Fang Wan and Rong-Shun Wang*

DOI: 10.1039/x0xx00000x

www.rsc.org/

A new cathode material composed of Romanechite-structural $\text{Na}_{0.31}\text{MnO}_{1.9}$ nanofibers is developed for sodium ion battery for the first time. It can deliver a Na-uptake capacity of $>100 \text{ mA h g}^{-1}$ with superior high-rate capabilities and good cycling performance in the voltage range of 2–4.5 V vs. Na^+/Na , and exhibit the unique ability of fast charge with the normal discharge rate.

With the very rapid development of energy storage, the large-scale usage of LIB will make the lithium sources be shortage in the near future.¹ In comparison to the very low abundance of about 0.0065% for lithium element, that for sodium element is up to about 2.83% in the earth's crust.² This imply that sodium ion battery (SIB) should be the most promising substitute with much lower cost if its properties reach the comparable level.³ Furthermore, SIB has some additional merits^{4, 5} such as environmental friendliness and large-scale usability. However, the radius (102 pm) of sodium ion is obviously larger than that (76 pm) of lithium ion, making that the crystalline lattices of most SIB's electrode materials will severely counter much huger volume variation compared to those of LIB during cycling. Hence, it is still a big challenge to develop the practicable electrodes with superior electrochemical properties.⁴

Amongst various cathode materials for SIB, the sodium manganese oxides (SMOs) are of great importance due to the existence of large interlayer distance or channel in their crystalline lattices, which can facilitate the intercalation/de-intercalation process of sodium ions.⁶ Moreover, all of the elements (sodium, manganese and oxygen) contained in the materials are non-toxic and fruitful, making them really large-scale usability. Thus, SMOs have been considered as one type of promising alternatives to the next generation cathodes of rechargeable SIB. So far, a lot of SMOs, such as $\text{Na}_{0.44}\text{MnO}_2$,⁷ $\text{Na}_{0.53}\text{MnO}_2$,⁸ $\text{Na}_{0.35}\text{MnO}_2$,⁹ $\text{Na}_{0.7}\text{MnO}_2$,¹⁰ $\text{Na}_{0.6}\text{MnO}_2$,¹¹

NaMnO_2 ¹² and NaMn_3O_5 ¹³ have been developed as cathode for SIB. However, most of them exhibit relatively poor rate and cycling performance. For example, their reversible capacities usually decreases to lower than 50% after 20–30 cycles.

Herein, one romanechite-structural sodium manganese oxide ($\text{Na}_{0.31}\text{MnO}_{1.9}$) with the shape of uniform nanofibers has been successfully prepared by combining the chelator-assisted precipitation and high-temperature sintering processes.¹⁴ Electrochemical test results disclose that it can deliver a sodium-storage capacity of $>100 \text{ mA h g}^{-1}$ with superior high-rate capabilities and good cycling performance. More excitingly, the $\text{Na}_{0.31}\text{MnO}_{1.9}$ nanofibers exhibit the ability of fast charging and slow discharging, which will be very important for practical application. Furthermore, the apparent diffusion coefficient of sodium ions in the crystalline lattices for the new $\text{Na}_{0.31}\text{MnO}_{1.9}$ cathode is also investigated by the technologies of electrochemical impedance spectroscopy (EIS) and galvanostatic intermittent titration technique (GITT).

The crystallographic structures of the prepared sodium manganese oxide (NMO) were firstly characterized by the power X-ray diffraction (XRD). Figure 1a shows its typical XRD pattern. It can be seen that all the peaks are well in agreement with the diffraction peaks of PDF#27-0749 card, indicating that the prepared NMO material is mainly composed of Romanechite-structural powdery crystals, except for a very weak diffraction peaks at about 22.5° due to the existence of small amount of impurity Mn_2O_3 (PDF#41-1442) as described in previously published papers.^{14, 15} Inset in Figure 1a is the schematic representation of Romanechite-structural NMO with lattice parameters of $a=13.81 \text{ \AA}$, $b=2.863 \text{ \AA}$ and $c=9.74 \text{ \AA}$. As disclosed, in this crystalline structure, there exist obvious (2×3) tunnel structures with sodium ions, which is constituted by MnO_6 octahedrons via sharing their corners and sides. The existed large-size tunnels will be very helpful to facilitate the Na^+ migration in it when used as cathode materials for SIB.

The morphology and size of the prepared NMO materials were further characterized by scanning electron microscopy (SEM). The typical SEM image for NMO is shown in Figure 1b,

^a National & Local United Engineering Laboratory for Power Batteries and Faculty of Chemistry, Northeast Normal University Changchun, Jilin 130024, P. R. China. E-mail: xinglong@nenu.edu.cn

Electronic Supplementary Information (ESI) available: [details of any supplementary information available should be included here]. See DOI: 10.1039/x0xx00000x

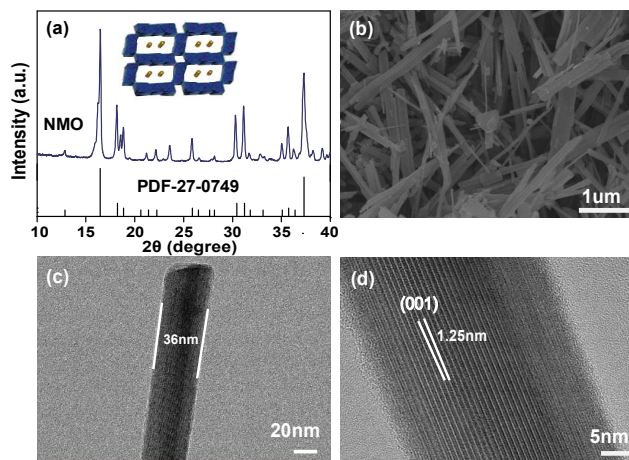


Figure 1. (a) XRD patterns of the as-prepared NMO materials. The inset is the schematic representation of romanechite structure. (b) Typical SEM image, (c) TEM and (d) HRTEM images of the NMO nanofibers.

disclosing that it is composed of uniform nanofibers with length of several micrometers and diameter of 20–40 nm. The image of transmission electron microscopy (TEM) in Figure 1c shows the tip of one single NMO nanofiber with diameter of 36 nm. Furthermore, the high-resolution TEM image (Figure 1d) clearly discloses the interlayer spacing of 1.25 nm of the $\text{Na}_{0.31}\text{MnO}_{1.9}$ nanofiber, corresponding to (001) fringes for the Romanechite-structural NMO.¹³ The energy-dispersive X-ray (EDX) spectroscopy (Figure S1) further discloses its elemental composition including only Na, Mn and O elements. Additionally, the Brunner–Emmet–Teller surface area of the as-prepared NMO is about $11.5 \text{ m}^2/\text{g}$, a low value, promising it to be a proper cathode material for practical application.

In addition to the crystallographic structure and shape, the chemical compositions of bulk and surface of the prepared NMO material are further obtained by inductively coupled plasma atomic emission spectroscopy (ICP-AES) and X-ray photoelectron spectroscopy (XPS) respectively. According to the calculation results for the ICP-AES tests showed in Table 1, the mole ratio of Na:Mn:O is about 0.31:1:1.9, which is consistent well with the feeding ratio of the sodium and manganese elements. This demonstrates that the chemical formula of the prepared NMO should be $\text{Na}_{0.31}\text{MnO}_{1.9}$. Figure 2 is the typical high-resolution XPS spectra of Mn, O and Na elements in the NMO material. As Figure 2a shows, the XPS of Mn2p is composed of two broad peaks centered at about 642.4 eV and 654.0 eV, which is attributable to the signals of $\text{Mn}2\text{p}^{3/2}$ and $\text{Mn}2\text{p}^{1/2}$ respectively.¹⁶ By fitting the Mn2p peaks, the binding energies for both Mn^{4+} and Mn^{3+} can be detected, demonstrating that the Mn element of the prepared NMO material is in the mixed valence states of Mn^{4+} and Mn^{3+} .¹⁷ Furthermore, the average valence of Mn atoms (V_{Mn}) in the prepared NMO material has also been calculated by the energy separation (ΔE_{3s} , as shown in Figure 2b) between two Mn_{3s} peaks, which is mainly originated from the coupling effect of non-ionized 3s electrons with 3d valence-band

electrons. Precisely, the ΔE_{3s} values are inversely proportional to the oxidation state of Mn atoms in the Mn-containing oxides.¹⁸ According to the following linear equation ($V_{\text{Mn}} = 7.875 - 0.893 \Delta E_{3s}$) between V_{Mn} and ΔE_{3s} , which was established by Kim and co-authors⁸, the surficial average valence V_{Mn} of the prepared NMO material can be calculated as +3.32 on the basis of $\Delta E_{3s} = 5.1 \text{ eV}$ as disclosed in Figure 2b. For the sodium manganese oxide ($\text{Na}_{0.31}\text{MnO}_{2+\delta}$) with ICP-AES-determined Na/Mn ratio of 0.31:1, the δ value can be further calculated as about -0.19, because the valence sum of all atoms will be zero in one compound. Hence, the surficial chemical formula of the prepared NMO materials should be $\text{Na}_{0.31}\text{MnO}_{1.81}$, in which the oxygen content is very similar with but slightly lower than that of bulk $\text{Na}_{0.31}\text{MnO}_{1.9}$. This implies that there exists a small amount (about 4.74%) of oxygen defects in the NMO's surface compared to the bulk one. Thereafter, the chemical formula of the prepared NMO materials will be still written as $\text{Na}_{0.31}\text{MnO}_{1.9}$ for convenience. In addition, the XPS peaks located at 529 eV and 532 eV as well as centered at 1071 eV, shown in Figures S2, can be attributed to the responses of O1s and Na1s¹⁹ respectively.

Moreover, various electrochemical technologies had been used to evaluate the Na-uptake of the $\text{Na}_{0.31}\text{MnO}_{1.9}$ nanofibers as cathode for SIB. Figure 3a firstly shows the cyclic voltammetry (CV) curves between 2 to 4.5 V vs. Na^+/Na at a scan rate of 0.1 mV s^{-1} . Except for the obviously different oxidation (desodiation) process in the first cycle, which should be attributed to the initial phase transition to accommodate the strain change during extraction of Na ions in the $\text{Na}_{0.31}\text{MnO}_{1.9}$ nanofibers,²⁰ the following cycles exhibit the almost completely overlapped CV curves, demonstrating the excellent reversibility of Na^+ insertion/extraction. In the CV curves, there exist at least four pairs of redox peaks, implying a complex multistep processes for the $\text{Na}_{0.31}\text{MnO}_{1.9}$ nanofibers during cycling as cathode for SIB.²¹ The strongest redox peaks located at around 2.67 V and 2.27 V vs. Na^+/Na should be related to the reaction of $\text{Mn}^{3+}/\text{Mn}^{4+}$ redox pair.²² At higher voltage window from 3.0–4.5 V vs. Na^+/Na , the other three pairs of peaks should be attributed to a multistep phase-transition process due to Na^+ insertion/desertion reactions.²⁰ Furthermore, the galvanostatic charge/discharge curves shown in illustration also exhibit the similar characteristic, viz. the curves tend to overlap after the first charging, also demonstrating the good reversibility and stability of the $\text{Na}_{0.31}\text{MnO}_{1.9}$ nanofibers during cycling. Figure 3b is the cycling

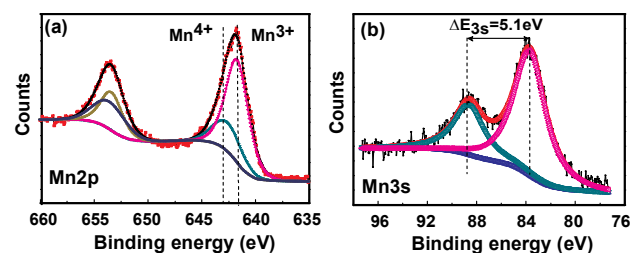


Figure 2. High-resolution XPS spectra of the prepared NMO material: (a) Mn2p, (b) Mn3s.

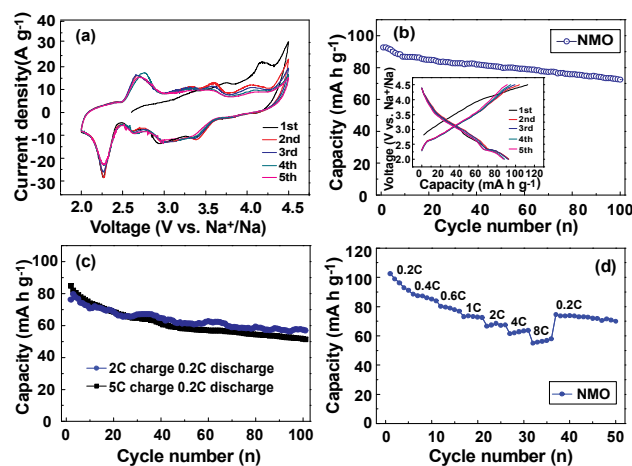


Figure 3. Electrochemical properties of the NMO nanofibers: (a) CV profiles, (b) cycling stability at the same charge and discharge rate of 1C, inset is galvanostatic charge/discharge curves cycled at a rate of 0.4C, (c) cycling performance at different charge/discharge rate, (d) the rate capabilities from 0.2C to 8C.

performance of $\text{Na}_{0.31}\text{MnO}_{1.9}$ nanofibers at 1C rate between 2–4.5 V vs. Na^+/Na . It can be clearly observed that the $\text{Na}_{0.31}\text{MnO}_{1.9}$ nanofibers exhibited a good cycling performance with a capacity retention of about 78.2% after 100 cycles. The less cycle stability should be originated from the undesirable Jahn-Teller distortion of Mn^{3+} and the severe volume changes due to the de/intercalation of large sodium ions.

In addition to the cycling performance cycled at the same charge and discharge rate, the prepared $\text{Na}_{0.31}\text{MnO}_{1.9}$ nanofibers interestingly exhibit the ability of fast charging. As shown in Figure 3c, the $\text{Na}_{0.31}\text{MnO}_{1.9}$ can charge at the high charge rates of 2C and 5C when discharged at a normal rate of 0.2C. For example, after 100 cycles, the capacity retentions are about 74.6% and 60.5 % for the charge rates of 2C and 5C respectively. This unique feature will be very helpful for its practical application of fast charge, and may be derived from its superior rate performance as shown in Figures 3d. In consistent with the cycling performance, the $\text{Na}_{0.31}\text{MnO}_{1.9}$ material exhibits the superior rate capability. For example, it can still deliver the reversible capacities of 76.8 mAhg^{-1} and 63.3 mAhg^{-1} at 1C and 8 C respectively. Note that, the delivered capacity could not well recover to the initial value when the current density returned to 0.2C. This may be originate from the disproportionation of Mn^{3+} into Mn^{4+} and dissolvable Mn^{2+} species.²³ Figure S3 is the discharge curves of the $\text{Na}_{0.31}\text{MnO}_{1.9}$ nanofibers at different rates from 0.2C to 8C. All the curves show the similar profiles, also demonstrating its superior rate performance²⁴. Additionally, at the low rate of 0.2C, the NMO materials can deliver higher reversible capacity compared to the theoretical value of about 89.9 mA h g^{-1} calculated from the molar ratio of Na element in the molecular formular of $\text{Na}_{0.31}\text{MnO}_{1.9}$. This implies that the present crystalline structure of Romanchite can uptake more sodium ions than the number already existed in the pristine crystal lattice in the following cycles.²³

The interfacial impedance and apparent Na^+ -diffusion of the NMO nanofiber was further explored by electrochemical impedance spectroscopy (EIS) technique. Figure 4a is the typical EIS Nyquist plot and the inset is the equivalent circuit used to fit this EIS plot. In the equivalent circuit, R_s represents the Ohmic resistance and solution resistance, R_{ct} is the charge transfer resistance between the electrolyte interface and electrode of Na^+ migration related to the semi-circles in the high frequency region, and C_{int} is the pseudo-capacitance at the interface between electrode and electrolyte.²⁵ In general, the sodium intercalation into the $\text{Na}_{0.31}\text{MnO}_{1.9}$ nanofibers is a complex multi-step processes, in which sodium ions will firstly migrate through the interface, and then insert into the electrode materials corresponding to R_{ct} and Na^+ -diffusion into the nanofibers.²⁵ The electro-chemical insertion/deinsertion does not a single solid solution mechanism, but a complex multiphase reactions process.⁷ Further, the straight line in the low frequency region is the Warburg behavior which was attributed to the diffusion of Na^+ in the electrode. We can evaluate the apparent Na^+ diffusion coefficient (D) of the $\text{Na}_{0.31}\text{MnO}_{1.9}$ nanofibers by the following equation 2 and 3:²⁶

$$D = (R^2 T^2) / (2A^2 n^4 F^4 C^2 \sigma^2) \quad (2)$$

$$Z_{re} = R_e + R_{ct} + \sigma \omega^{-1/2} \quad (3)$$

The linear fitting according to equation 3 for the low frequency region of the EIS plots shows in Figure 4b, from which the slope of the fitting line is 461.5. According to equation 2, it can be calculated that the D value is about $1.13 \times 10^{-14} \text{ cm}^2 \text{ s}^{-1}$, which is the same order of magnitude as the values obtained from the galvanostatic intermittent titration technique (GITT) as disclosed below. In addition to the EIS tests to determine the apparent Na^+ diffusion coefficient, GITT was further used to calculate the real-time ones in the desodiation processes in the whole voltage window from 2.0 V to 4.5 V vs. Na^+/Na .¹³

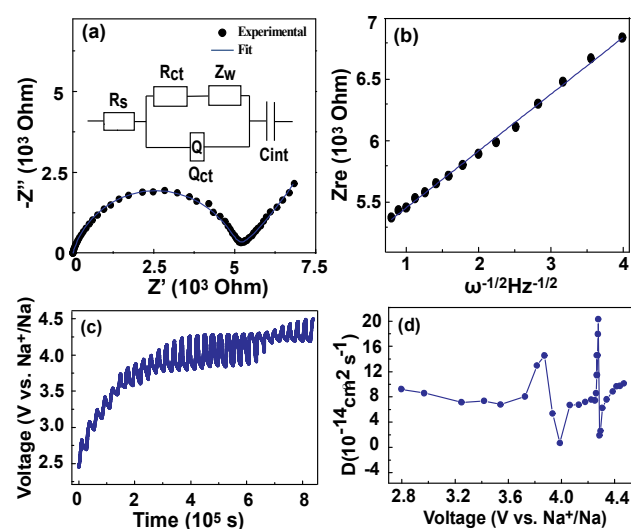


Figure 4. (a) EIS Nyquist plots of the NMO nanofibers; the inset is the equivalent circuit employed to fit the EIS plots. (b) Dependence of Z_{re} on the reciprocal square root of the frequency in the low-frequency region of the NMO nanofibers. (c) The whole GITT curve for the NMO electrode between 2.45 V and 4.5 V. (d) The variation of Na^+ diffusion coefficients along with the voltage.

The GITT tests were implemented at a constant rate of 0.05 C and the balance time of charging 3 hours and relaxing 4.5 hours.¹³ The Na⁺ diffusion coefficients D can be obtained by fitting each segment of voltage relaxation curves according to the following diffusion equation:

$$\ln\{F/RT[\exp(\varphi-\varphi_{\infty})-1]\} = -\ln N - 4.49^2/r_0^2 D t \quad (4)$$

The diffusion coefficient D reveals the dynamic equilibrium speed, which is determined by the kinetics process of phase change boundary movement. Figure S4a is one single titration curve of the Na_{0.31}MnO_{1.9} electrode charged to 2.7 V vs. Na⁺/Na. And the corresponding linear fitting result is shown in Figure S4b, from which the D value can be calculated according to equation 4. In addition, the whole GITT curve of the first desodiation process between 2.45 V and 4.5 V and the variation of Na⁺ diffusion coefficients along with the voltage are disclosed in Figures 4c and 4d respectively. The long platform at about 3.7-4.4 V vs. Na⁺/Na can be attributed to the desodiation from the lattice and oxidation reaction of Mn atoms, which is well consistent with the first oxidation and charge curves in the CV pattern and galvanostatic profile as shown in Figures 3a and 3b respectively. Note that, there is two relatively large deviations at the voltage windows of 3.7-4 V and 4.3-4.4 V, which corresponds to the two oxidation peaks of the first desodiation process in the CV pattern respectively. This deviation of D values at the phase-transition process (i.e. the position of redox peaks in the CV patterns) is a common phenomenon because of the co-occurrence of both Na⁺ diffusion and the transformation of crystalline structures.²⁷ The variations of crystalline species are also monitored by the ex-situ XRD investigation upon Na_{0.31}MnO_{1.9} desodiation from 3.7 V to 4.4 V with the interval of 0.1 V per test. Figure S5 shows all the XRD patterns which are discussed in the Supporting Information, and the corresponding results are well consistent with the above GITT tests. Therefore, all above results from CV, galvanostatic cycling, EIS, GITT and ex-situ XRD demonstrate that it is a complex dynamic process of electrochemical sodiation/ desodiation.

In summary, a new material of Na_{0.31}MnO_{1.9} nanofibers with Romanechite crystalline structure has been prepared as high-performance cathode for sodium ion battery. The as-prepared Na_{0.31}MnO_{1.9} nanofibers exhibit superior high-rate capabilities and good cycling performance. Its ability of fast charge and slow discharge can promote its practical application for sodium ion battery. In addition, the investigation of sodium ion diffusion by EIS and GITT demonstrates that the whole desodiation process is a complex dynamic process, which contains not only a simple Na⁺ diffusion but also the structural transformation. Further research of improving the cycling performance and the reaction mechanism are in progress.

This work was supported by the Science Technology Program of Jilin Province (20150520027JH, 20140101087JC), the Fundamental Research Funds for the Central Universities (14QNJJ014), and National High Technology Research and Development Program of China (2013AA110103). XL thanks the support of the International Postdoctoral Exchange Fellowship Program.

Notes and references

1. L. Zhao, Y. S. Hu, H. Li, Z. Wang and L. Chen, *Adv. Mater.*, 2011, **23**, 1385-1388.
2. Y. Yue, A. J. Binder, B. Guo, Z. Zhang, Z. A. Qiao, C. Tian and S. Dai, *Angew. Chem. Ed. Int.*, 2014, **53**, 3134-3137.
3. H. Pan, Y.-S. Hu and L. Chen, *Energy Environ. Sci.*, 2013, **6**, 2338.
4. Y. You, X. L. Wu, Y. X. Yin and Y. G. Guo, *Energy Environ. Sci.*, 2014, **7**, 1643-1647.
5. J. Ming, H. Ming, W. Yang, W.-J. Kwak, J.-B. Park, J. Zheng and Y.-K. Sun, *RSC Adv.*, 2015, **5**, 8793-8800.
6. N. Yabuuchi, K. Kubota, M. Dahbi and S. Komaba, *Chem. Rev.*, 2014, **114**, 11636-11682.
7. R. Ruffo, R. Fathi, D. J. Kim, Y. H. Jung, C. M. Mari and D. K. Kim, *Electrochim. Acta*, 2013, **108**, 575-582.
8. J. Song, J. Gim, S. Kim, J. Kang, V. Mathew, D. Ahn and J. Kim, *Chem. Asian J.*, 2014, **9**, 1550-1556.
9. B. H. Zhang, Y. Liu, Z. Chang, Y. Q. Yang, Z. B. Wen, Y. P. Wu and R. Holze, *J. Power Sources*, 2014, **253**, 98-103.
10. D. Su, C. Wang, H.-j. Ahn and G. Wang, *Chem.-Eur. J.*, 2013, **19**, 10884-10889.
11. A. Caballero, L. Hernán, J. Morales, L. Sánchez, J. Santos Peña and M. A. G. Aranda, *J. Mater. Chem.*, 2002, **12**, 1142-1147.
12. N. Bucher, S. Hartung, A. Nagasubramanian, Y. L. Cheah, H. E. Hoster and S. Madhavi, *ACS Appl. Mater. Inter.*, 2014, **6**, 8059-8065.
13. S. Guo, H. Yu, Z. Jian, P. Liu, Y. Zhu, X. Guo, M. Chen, M. Ishida and H. Zhou, *ChemSusChem*, 2014, **7**, 2115-2119.
14. S. Liu, C.-Z. Fan, Y. Zhang, C.-H. Li and X.-Z. You, *J. Power Sources*, 2011, **196**, 10502-10506.
15. F. Hu and M. M. Doeff, *J. Power Sources*, 2004, **129**, 296-302.
16. Y. Sun, X. Hu, W. Luo, F. Xia and Y. Huang, *Adv. Func. Mater.*, 2013, **23**, 2436-2444.
17. D.-W. Han, J.-H. Ku, R.-H. Kim, D.-J. Yun, S.-S. Lee and S.-G. Doo, *ChemSusChem*, 2014, **7**, 1870-1875.
18. M. Toupin, T. Brousse and D. Bélanger, *Chem. Mater.*, 2004, **16**, 3184-3190.
19. M. Kalapsazova, R. Stoyanova and E. Zhecheva, *J. Solid State Electr.*, 2014, **18**, 2343-2350.
20. S. Doubajji, M. Valvo, I. Saadoune, M. Dahbi and K. Edstrom, *J. Power Sources*, 2014, **266**, 275-281.
21. S. P. Ong, V. L. Chevrier, G. Hautier, A. Jain, C. Moore, S. Kim, X. Ma and G. Ceder, *Energy Environ. Sci.*, 2011, **4**, 3680.
22. D. Buchholz, L. G. Chagas, C. Vaalma, L. M. Wu and S. Passerini, *J. Mater. Chem. A*, 2014, **2**, 13415-13421.
23. D. D. Yuan, Y. X. Wang, Y. L. Cao, X. P. Ai and H. X. Yang, *ACS Appl. Mater. Inter.*, 2015, **7**, 8585-8591.
24. X.-L. Wu, L.-Y. Jiang, F.-F. Cao, Y.-G. Guo and L.-J. Wan, *Adv. Mater.*, 2009, **21**, 2710-2714.
25. D. J. Kim, R. Ponraj, A. G. Kannan, H.-W. Lee, R. Fathi, R. Ruffo, C. M. Mari and D. K. Kim, *J. Power Sources*, 2013, **244**, 758-763.
26. X.-L. Wu, Y.-G. Guo, J. Su, J.-W. Xiong, Y.-L. Zhang and L.-J. Wan, *Adv. Energy Mater.*, 2013, **3**, 1155-1160.
27. M. H. Han, E. Gonzalo, G. Singh and T. Rojo, *Energy Environ. Sci.*, 2015, **8**, 81-102.